ISSN 1674-1056
http://cpb.iphy.ac.cn
http://iopscience.iop.org/cpb
中国物理 B
Chinese Physics
中国物理 Chinese Physics B

Estimation of vector static magnetic field by an nitrogen-vacancy center with a single first-shell ^{13}C nuclear (NV-^{13}C) spin in diamond

Feng-Jian Jiang(蒋峰建), Jian-Feng Ye(叶剑锋), Zheng Jiao(焦铮), Zhi-Yong Huang(黄志永), Hai-Jiang Lv(吕海江)
Citation: Chin. Phys. B . 2018, 27(5): 057601. **doi:** 10.1088/1674-1056/27/5/057601

Journal homepage: http://cpb.iphy.ac.cn; http://iopscience.iop.org/cpb

What follows is a list of articles you may be interested in

Experimental investigation of vector static magnetic field detection using an NV center with a singlefirst-shell ^{13}C nuclear spin in diamond

Feng-Jian Jiang(蒋峰建), Jian-Feng Ye(叶剑锋), Zheng Jiao(焦铮), Jun Jiang(蒋军), Kun Ma(马堃), Xin-Hu Yan(闫新虎), Hai-Jiang Lv(吕海江)
Chin. Phys. B . 2018, 27(5): 057602. **doi:** 10.1088/1674-1056/27/5/057602

A dual-axis, high-sensitivity atomic magnetometer

Rujie Li(李茹杰), Wei Quan(全伟), Wenfeng Fan(范文峰), Li Xing(邢力), Zhuo Wang(王卓), Yueyang Zhai(翟跃阳), Jiancheng Fang(房建成)
Chin. Phys. B . 2017, 26(12): 120702. **doi:** 10.1088/1674-1056/26/12/120702

Spin dynamics of magnetic resonance with parametric modulation in a potassium vapor cell

Rui Zhang(张锐), Zhi-Guo Wang(汪之国), Xiang Peng(彭翔), Wen-Hao Li(黎文浩), Song-Jian Li(李松健), Hong Guo(郭弘)
Chin. Phys. B . 2017, 26(3): 030701. **doi:** 10.1088/1674-1056/26/3/030701

In-situ measurement of magnetic field gradient in a magnetic shield by a spin-exchange relaxation-free magnetometer

Fang Jian-Cheng, Wang Tao, Zhang Hong, Li Yang, Cai Hong-Wei
Chin. Phys. B . 2015, 24(6): 060702. **doi:** 10.1088/1674-1056/24/6/060702

A laser pump-re-pump atomic magnetometer

Yang Ai-Lin, Yang Guo-Qing, Cai Xun-Ming, Xu Yun-Fei, Lin Qiang
Chin. Phys. B . 2013, 22(12): 120702. **doi:** 10.1088/1674-1056/22/12/120702

Estimation of vector static magnetic field by a nitrogen-vacancy center with a single first-shell ^{13}C nuclear (NV–^{13}C) spin in diamond*

Feng-Jian Jiang(蒋峰建)†, Jian-Feng Ye(叶剑锋), Zheng Jiao(焦铮), Zhi-Yong Huang(黄志永), and Hai-Jiang Lv(吕海江)‡

School of Information Engineering, Huangshan University, Huangshan 245041, *China*

(Received 22 March 2018; published online 26 April 2018)

We suggest an experimental scheme that a single nitrogen-vacancy (NV) center coupled to a nearest neighbor ^{13}C nucleus as a sensor in diamond can be used to detect a static vector magnetic field. By means of optical detection magnetic resonance (ODMR) technique, both the strength and the direction of the vector field could be determined by relevant resonance frequencies of continuous wave (CW) and Ramsey spectrums. In addition, we give a method that determines the unique one of eight possible hyperfine tensors for an (NV–^{13}C) system. Finally, we propose an unambiguous method to exclude the symmetrical solution from eight possible vector fields, which correspond to nearly identical resonance frequencies due to their mirror symmetry about ^{14}N–Vacancy–^{13}C (^{14}N–V–^{13}C) plane.

Keywords: color centers, optical detection magnetic resonance (ODMR), magnetometer

PACS: 76.70.Hb, 76.30.Mi, 07.55.Ge **DOI:** 10.1088/1674-1056/27/5/057601

1. Introduction

The negatively charged nitrogen-vacancy (NV) color center[1,2] in diamond has attracted great interest from various quantum information processing (QIP) applications[3–8] to high-resolution sensing of magnetic field[9,10] and imaging in life science[11] by using ODMR technique,[12] even at room temperature. Specifically, NV center has become a prominent magnetometer, the central idea of which is detecting the relative energy shift of ground state by an external AC or DC vector magnetic field.[9,10,13,14] By detecting frequency and relevant shift, the corresponding parameters of external magnetic field could be precisely determined. The information of strength and polar angle of vector magnetic field (relative to NV symmetry axis) could be easily extracted by observing two resonance frequencies of continuous wave (CW) spectrums, but the information of azimuth angle is still missing due to the C_{3v} symmetry of the defect. One solution to this issue is that NVs were employed in a multi-NV vector magnetometer with different [111] axes.[13,15] However, these NVs are the best to be close to each other and differ by no more than hundreds of nanometers for achieving high spatial resolution. Another alternative strategy, suggested theoretically by Ref. [16], only used a single high-spin system (such as SiC with spin 3/2) as a vector magnetometer, which might further improve the spatial resolution.

In this paper, using a single NV center with a single first-shell ^{13}C nuclear spin (NV–^{13}C), an executable experiment scheme of detecting a static vector magnetic field is proposed in diamond. More information of vector magnetic field could be revealed by resonance spectrum. The reason is that the symmetry of the NV–^{13}C can be reduced from C_{3V} to C_S, a single mirror plane. Moreover, the energy level splitting of ^{13}C nuclear spin is sensitive to the changes of external magnetic field in contrast to ^{14}N nuclear spin, which remains almost unchanged. Due to the distance between ^{13}C nucleus and NV electron less than 1 nm, the advantage of our proposal is that high spatial resolution conditioning precise measured hyperfine coupling tensor of NV–^{13}C,[17–21] high contrast of the fluorescent readout, and narrow linewidth of resonance spectrum lines[22] may be achieved by experimental implementation.

2. A static vector magnetic field detection with an NV–^{13}C

2.1. The NV–^{13}C system

An NV–^{13}C sensor consists of a substitutional ^{14}N and a nearest neighbor ^{13}C nuclear spins adjacent to the vacancy defect. The spin Hamiltonian of the system under an applied static vector magnetic field $\boldsymbol{B}$ can be written in a coordinate system, in which the NV axis is aligned to z axis, and x axis lies in the plane constructed by ^{14}N–V–^{13}C (seen in Fig. 1).

*Protect supported by the National Natural Science Foundation of China (Grant Nos. 11305074, 11135002, and 11275083), the Key Program of the Education Department Outstanding Youth Foundation of Anhui Province, China (Grant No. gxyqZD2017080), and the Natural Science Foundation of Anhui Province, China (Grant No. KJHS2015B09).

†Corresponding author. E-mail: jfjiang@mail.ustc.edu.cn

‡Corresponding author. E-mail: luhj9404@mail.ustc.edu.cn

© 2018 Chinese Physical Society and IOP Publishing Ltd

The combined spin system can be written by Hamiltonian

$$\mathcal{H}_{\rm tot} = DS_z^2 + \gamma_{\rm e}\boldsymbol{B}\cdot\boldsymbol{S} + P(I_z^{^{14}\rm N})^2 + \gamma_{\rm n}^{^{14}\rm N}\boldsymbol{B}\cdot\boldsymbol{I}^{^{14}\rm N} + \gamma_{\rm n}^{^{13}\rm C}\boldsymbol{B}\cdot\boldsymbol{I}^{^{13}\rm C} + \mathcal{H}_{\rm hf}^{^{14}\rm N} + \mathcal{H}_{\rm hf}^{^{13}\rm C}, \quad (1)$$

where vector magnetic field $\boldsymbol{B}$ can be expended to $\boldsymbol{B}(\sin\theta\cos\phi\hat{\boldsymbol{x}}, \sin\theta\sin\phi\hat{\boldsymbol{y}}, \cos\theta\hat{\boldsymbol{z}})$, θ and ϕ are the polar and the azimuth angles relative to z and x axes in the NV frame of reference, respectively. The gyromagnetic ratios of NV electron, ^{13}C and ^{14}N nuclear spins are $\gamma_{\rm e} = 2.8$ MHz$\cdot$G^{-1}, $\gamma_{\rm n}^{^{13}\rm C} = -0.00107$ MHz$\cdot$G^{-1}, and $\gamma_{\rm n}^{^{14}\rm N} = 0.43$ kHz$\cdot$G^{-1}, respectively. Zero-field splitting D and quadrupole splitting P of ^{14}N correspond to 2.87 GHz and -5 MHz, respectively. The last two terms of Eq. (1) respectively represent the NV electron spin coupled to ^{14}N and proximal ^{13}C nuclear spin. Since the hyperfine splitting of ^{14}N nuclear spin (spin $I = 1$) is a constant of -2.16 MHz[23] and insensitive to changes of applied vector magnetic field, we could only consider the hyperfine structure of NV spin coupled to the ^{13}C nucleus written as

$$\mathcal{H}_{\rm NV-^{13}C} = DS_z^2 + \gamma_{\rm e}\boldsymbol{B}\cdot\boldsymbol{S} + \gamma_{\rm n}^{^{13}\rm C}\boldsymbol{B}\cdot\boldsymbol{I}^{^{13}\rm C} + \boldsymbol{S}\cdot\boldsymbol{A}\cdot\boldsymbol{I}^{^{13}\rm C}, \quad (2)$$

where the NV–^{13}C hyperfine interaction $\mathcal{H}_{\rm hf}^{^{13}\rm C}$ is $\boldsymbol{S}\cdot\boldsymbol{A}\cdot\boldsymbol{I}^{^{13}\rm C} = A_{xx}S_xI_x + A_{yy}S_yI_y + A_{zz}S_zI_z + A_{xz}S_zI_x + A_{zx}S_xI_z$, when choosing the x axis such that $A_{zy} = A_{yz} = 0$ without lack of generality. From Eq. (2), eigenvalues E_i $(i = 1,\ldots,6)$ in descending order and corresponding eigenvectors $|E_i\rangle$ of ground state can be obtained. For sub-manifold $m_{\rm s} = \pm1$ with the hyperfine splitting of ^{13}C nuclear spin, the relevant eigenvectors $|E_{1,2,3,4}\rangle$ could be approximately equal to $|\ell,\alpha_k\rangle$ ($\ell = \pm1$ and $k = \pm$), where the ^{13}C nuclear spin states $|\alpha_\pm\rangle$ could be approximated as $|\alpha_\pm\rangle \approx \cos\frac{\vartheta}{2}|+\rangle \pm \sin\frac{\vartheta}{2}|-\rangle$ with $\tan\vartheta = A_{xz}/A_{zz}$.[24] The ordering of the corresponding energy level of eigenvectors $|\pm1,\alpha_\pm\rangle$ could be exchanged by the switching of polar angle θ between $(0,\pi/2)$ and $(\pi/2,\pi)$. For sub-manifold $m_{\rm s} = 0$, its corresponding eigenvectors $|E_{5,6}\rangle$ could be approximately equal to $|0,\beta_\pm\rangle$, in which the nuclear states $|\beta_\pm\rangle$ of interest depended entirely on applied vector magnetic field and could be written as $|\beta_\pm\rangle = \cos\frac{\theta}{2}|m_I = +1/2\rangle \pm {\rm e}^{{\rm i}\phi}\sin\frac{\theta}{2}|m_I = -1/2\rangle$.

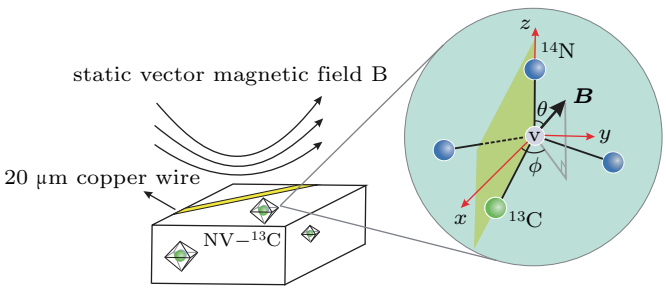


Fig. 1. (color online) A static vector magnetic field $\boldsymbol{B}$ is applied. NV–^{13}C frame of reference is defined by x, y, z axes, where ϕ and θ represent the azimuth and the polar angles with respect to the x and z axes, respectively.

Concrete schematic diagram can refer to Appendix A. Specifically, the quantization axis of sub-manifold $m_{\rm s} = 0$ and corresponding spin dynamics could be affected by the microwave power strength.

2.2. The determination of eight candidated hyperfine tensors for a single NV–^{13}C

In the NV–^{13}C frame of reference, the symmetric hyperfine tensor

$$\boldsymbol{A} = \begin{pmatrix} A_{xx} & 0 & A_{xz} \\ 0 & A_{yy} & 0 \\ A_{zx} & 0 & A_{zz} \end{pmatrix} \text{MHz},$$

associated with the nearest ^{13}C coupled to NV spin, was determined in Ref. [19], where $A_{i,j}$ for $i,j = x,y,z$ is the component of eight candidated hyperfine tensors, $\boldsymbol{A}$. The components are listed in Appendix B, in which the signs of $A_{xz} = A_{zx}$ can be positive or negative, and can be linked by a π rotation transformation around the z axis.

However, when NV–^{13}C is used as a vector magnetometer, its hyperfine tensor should be uniquely identified instead of multiple candidates due to mirror symmetry. A simple scheme may be feasible as an initial state of NV electron spin $(|m_{\rm s} = 0\rangle + |m_{\rm s} = -1\rangle)/\sqrt{2}$ with ^{13}C nuclear spin state $(|m_I = +1/2\rangle + |m_I = -1/2\rangle)/\sqrt{2}$ is polarized[1,24] and prepared. Under an applied magnetic field $\boldsymbol{B}$ aligned along the NV–^{13}C axis (z-axis), its total free evolution under the Hamiltonian (2) demonstrates eight different evolution processes conditioned the chosen hyperfine tensor. The evolving states are projected onto the state $|m_{\rm s} = -1\rangle \otimes |m_I = -1/2\rangle$ with evolving populations as shown in Fig. 2. Along the way, in experiment one needs to observe the free induction decay (FID) signal of the NV–^{13}C.

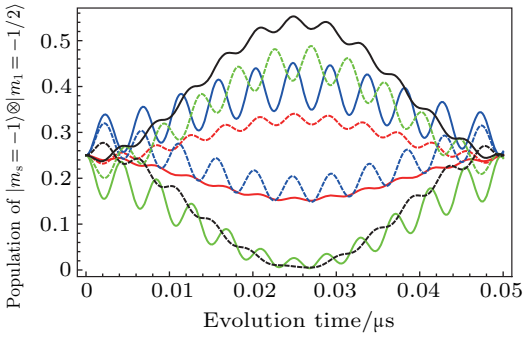


Fig. 2. (color online) The applied external magnetic $\boldsymbol{B} = 510$ Gs is parallel to the NV axis. Red and dashed red lines correspond to hyperfine tensor $\boldsymbol{A}_1$ with $A_{zx} = -24.1$ MHz and $A_{zx} = +24.1$ MHz, respectively. Blue and dashed blue lines correspond to hyperfine tensor $\boldsymbol{A}_2$ with $A_{zx} = -24.1$ MHz and $A_{zx} = +24.1$ MHz, respectively. Green and dashed green lines correspond to hyperfine tensor $\boldsymbol{A}_3$ with $A_{zx} = +99.3$ MHz and $A_{zx} = -99.3$ MHz, respectively. Black and dashed black lines correspond to hyperfine tensor $\boldsymbol{A}_4$ with $A_{zx} = +99.3$ MHz and $A_{zx} = -99.3$ MHz, respectively.

2.3. The spin dynamics of ground state under microwave field

A microwave (MW) field is applied and causes transitions between the electron spin levels, which modulates the fluorescence intensity. At relative low microwave power, the hyperfine splitting of $m_s = 0$ corresponds to two eigenstates of $|0,\beta_+\rangle$ and $|0,\beta_-\rangle$, between which the analytic form

$$\Delta \approx \frac{2|\gamma_e B \sin\theta|}{D}\left(\sqrt{A_{xx}^2 + A_{zx}^2}\cos^2\phi + |A_{yy}|\sin^2\phi\right)$$

of the effective Larmor splitting obtained by the second order perturbation theory reveals the direction of applied vector field.[18] Through numerical calculations in moderate magnetic field ($\lesssim 100$ Gs), the above approximate formula of Δ conforms well to the numerical results based on Eq. (2). In the remaining cases of relatively high MW power, the Larmor splitting of sub-manifold $m_s = 0$ corresponds to two linear superposition states $|0,\alpha_\pm\rangle$ of eigenstates $|0,\beta_+\rangle$ and $|0,\beta_-\rangle$, whose quantization axis of nuclear spin is realigned to a new axis defined by nuclear spin states $|\alpha_\pm\rangle$.[24]

At relatively low MW power, the doublet transitions between $|0,\beta_\pm\rangle$ and $|\ell,\alpha_k\rangle$ could be observed. Taking into account the hyperfine splitting of the ^{14}N nucleus, the double peak transitions above could further show six resonance lines as demonstrated schematically in Fig. 4(a). With the increase of MW power, only a single peak transition could be observed and its resonance frequency is almost centred between the doublet transitions of $|0,\beta_\pm\rangle \leftrightarrow |\ell,\alpha_k\rangle$ as shown in Fig. 4(b).

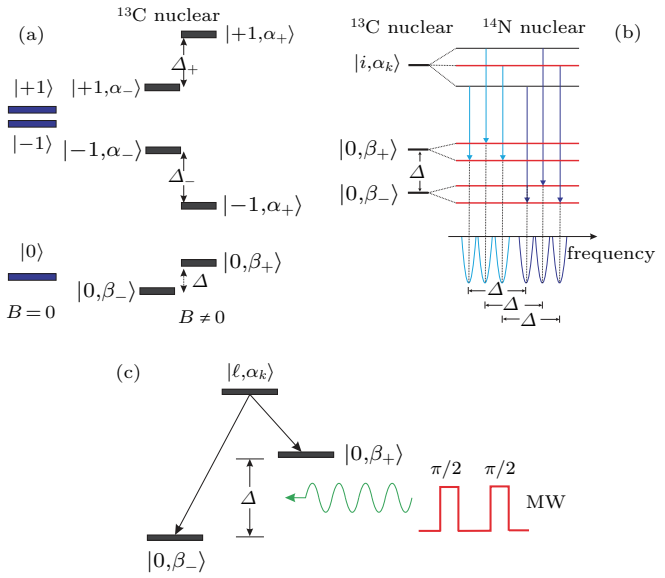


Fig. 3. (color online) (a) The energy-level diagram of NV–^{13}C center ground state. The hyperfine splitting of Δ and $\Delta_\pm$ correspond to $m_s = 0$ and $m_s = \pm 1$ ground-state manifolds due to coupled to the nearest ^{13}C nuclear spin. (b) Under the low power microwave, six resonance peaks could be observed due to the hyperfine interaction between electron and ^{14}N nuclear spin. (c) Ramsey sequence for detecting the Larmor splitting Δ. Notations are defined in the main text.

2.4. Numerical simulations of a static vector magnetic field detection

2.4.1. Simulation ODMR spectra of the NV–^{13}C system

NV center can be optically addressed at room temperature using a confocal microscope combined with a photon-counting detection system.[12] An external static vector magnetic field whose direction is relative to the NV–^{13}C of interest is shown schematically in Fig. 1.

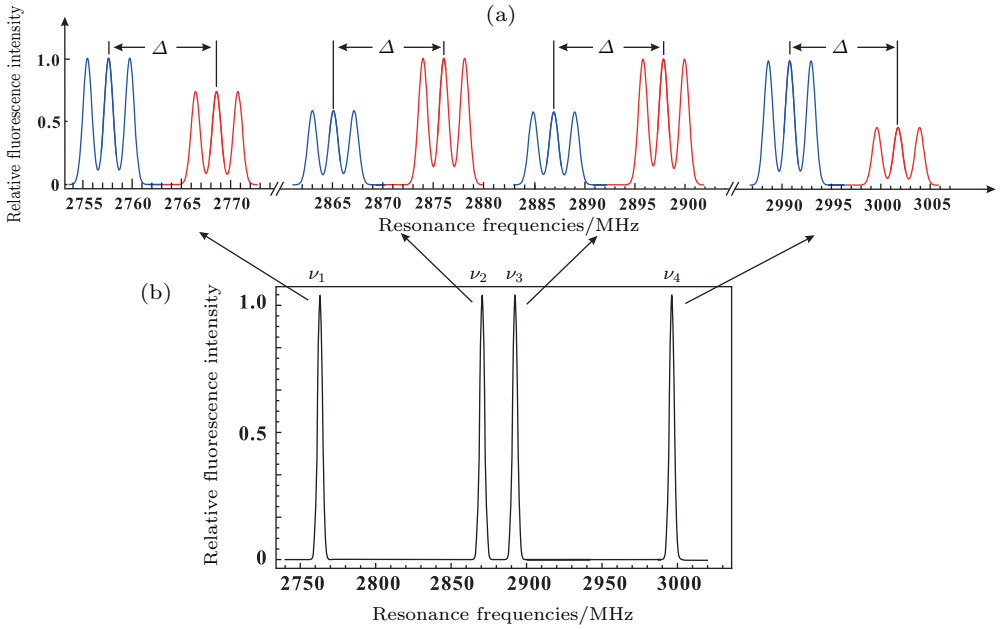


Fig. 4. (color online) As an example, ODMR CW spectra was simulated with $\boldsymbol{A}_1(A_{zx} = -24.1$ MHz) for preset parameters $\theta = 57°$, $\phi = (11°, 169°, 191°,$ or $349°)$, and $\boldsymbol{B} = 35$ Gs satisfying mirror symmetry about ^{14}N–V–^{13}C plane. (a) The relatively low MW power reveals doublet transitions of each resonance line in panel (b). The 24 resonance lines resulted from the ^{13}C nucleus and the fixed splitting (2.16 MHz) were induced by ^{14}N nucleus. The asymmetry of 24 resonance lines is due to the different transition probabilities between $|0,\beta_+\rangle \leftrightarrow |\ell,\alpha_k\rangle$ and $|0,\beta_-\rangle \leftrightarrow |\ell,\alpha_k\rangle$. (b) At relatively high MW power, the NV–^{13}C indicates four resonance spectral lines due to hyperfine coupling with the ^{13}C nucleus. Notations are defined in the main text.

In the following, these frequency hyperfine magnetic resonance lines could be observed by pulsed CW ODMR spectra. The corresponding four resonance frequencies $\nu_{1,2,3,4}$ and the Larmor splitting Δ could be obtained as simulated in Fig. 4. For more precise measurement, the Larmor splitting could also be obtained by using Ramsey-type sequence $\pi/2-\tau-\pi/2$.[25] The spectrum in Fig. 4(a) shows 24 resonance peaks due to the coupling with the ^{14}N nucleus. The fluorescence intensities of 24 spectral lines in Fig. 4 are commonly asymmetry. The reason is mainly that the doublet transition probabilities between $|0,\beta_+\rangle \leftrightarrow |\ell,\alpha_k\rangle$ and $|0,\beta_-\rangle \leftrightarrow |\ell,\alpha_k\rangle$ are different. Based on the calculations of MW transition matrix elements $|\langle E_i|S_x|E_j\rangle|^2$ with $j=1,2,3,4$ and $i=5,6$, the change of the relative fluorescence intensities for the doublet transition depends on the polar angle θ of the vector field. Qualitative analysis can refer to Appendix C. It should be noted that if the magnetic field is higher than 200 Gs, the fluorescence of the NV center would be dramatically influenced and could not be measured by the CW spectrum.

2.4.2. The fault tolerance analysis of NV–^{13}C sensor

The four resonance frequencies $\nu_{1,2,3,4}$ of electron spin are sensitive to the changes of polar angle θ, compared to its insensitivity of the changes of azimuth angle ϕ. However, the Larmor splitting Δ induced by ^{13}C nuclear spin is sensitive to the changes of ϕ as shown in Fig. 5. Thus, to precisely detect a static vector magnetic field, both the two factors of $\nu_{1,2,3,4}$ and Δ should be taken into consideration.

With a method akin to maximum likelihood estimation, our simulations implemented a numerical search procedure to match both the target four measured resonance frequencies $\nu_{1,2,3,4}$ and the measured Larmor splitting Δ as shown in Fig. 4 according to the formula similar to[13]

$$\xi_1(\theta,\phi,\boldsymbol{B}) = \sum_{i=1,2,3,4} |E_i-(E_5+E_6)/2-(\nu_i+\epsilon_{\nu_i})| + |E_5-E_6-(\Delta+\epsilon_\Delta)|, \quad (3)$$

where the $\nu_{1,2,3,4}$ and Δ have linewidth $\delta\nu_i$ and $\delta\Delta$, respectively. The linewidth δ is fundamentally limited by the imhomogeneous dephasing rate, $\propto 1/T_2^*$ of the NV electron spin, which is decided by magnetic dipolar interactions with a bath of nuclear spin in diamond. The pulsed-ESR spectrum linewidth $\delta\nu_i$ is inversely proportional to the π-pulse duration limited by T_2^*. Furthermore, the linewidth could also be affected by power broadening, which is from the laser used for initializing electron spin and MW field used for spin manipulation. Thus, in experiment, the laser intensity and MW power should be decreased appropriately for achieving a sharpen linewidth.[22] For Larmor splitting Δ, Ramesy sequence could achieve sharper linewidth $\delta\Delta \sim$ kHz. Therefore, we introduced random measurement errors $\epsilon_{\nu_i} \in [-\delta\nu/2, \delta\nu/2]$ and $\epsilon_\Delta \in [-\delta\Delta/2, \delta\Delta/2]$ limited by linewidth $\delta\nu_i$ and $\delta\Delta$. One could pick the parameters θ_0, ϕ_0, and B_0 satisfying

$$\xi_{\min}(\theta_0,\phi_0,B_0) = \min_{\theta,\phi,B} \xi(\theta,\phi,B), \quad (4)$$

that minimizes Eq. (3), compared to other choices of parameters. The search ranges of direction parameters (θ,ϕ) are set to $[0,\pi]$ and $[0,2\pi]$, respectively.

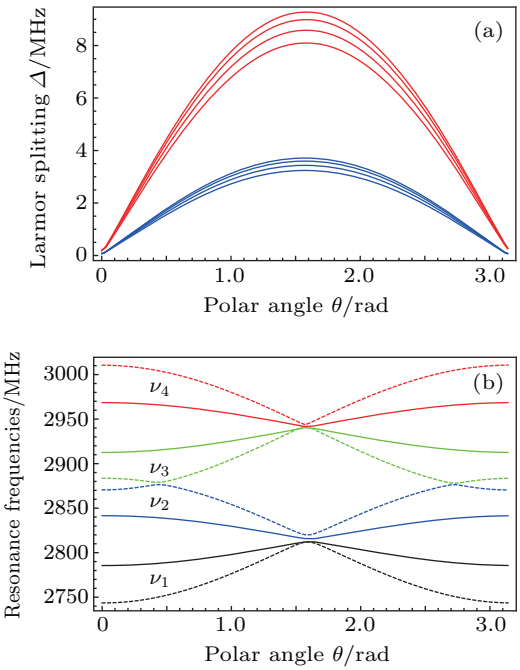


Fig. 5. (color online) (a) Red and blue lines correspond to the cases of $\boldsymbol{B}=20$ Gs and $\boldsymbol{B}=10$ Gs, respectively. The four curves of each group (red or blue lines) associated with Larmor splittings Δ correspond to fixed four azimuth angles $\phi=3\pi/36, 5\pi/36, 7\pi/36$ and $9\pi/36$, which can be distinguished by changes of Δ (at least ~ 100 kHz/0.1 rad) for relatively large misalignment angle θ relative to the z axis. (b) Dashed and solid lines correspond to the cases of $\boldsymbol{B}=20$ Gs and $\boldsymbol{B}=10$ Gs respectively. The four resonance frequencies $\nu_{1,2,3,4}$ of each group (dashed or solid lines) are sensitive and insensitive to the changes of θ and ϕ, respectively. In contrast to panel (a), the resonance frequencies $\nu_{1,2,3,4}$ are almost unchanged (at most ~ 2 kHz/0.1 rad) for the chosen fixed four different azimuth angles $\phi=3\pi/36$, $5\pi/36$, $7\pi/36$, and $9\pi/36$. Notations are defined in the main text.

With above method, the simulations of detecting vector direction with fixed $\boldsymbol{B}$ are carried out and results are given in Fig. 6, where random measurement errors ϵ_{ν_i} and ϵ_Δ are introduced. It should be noted that for large misalignment angle θ relative to the z axis, high resolution of azimuth angle ϕ may be easily achieved compared to those of small misalignment angle θ. At the same time, relatively higher magnetic field strength could improve the angular resolution of detected $\boldsymbol{B}$ due to the higher resolution of Larmor splitting Δ for different azimuth angles ϕ as shown in Figs. 5(a) and 6(c).

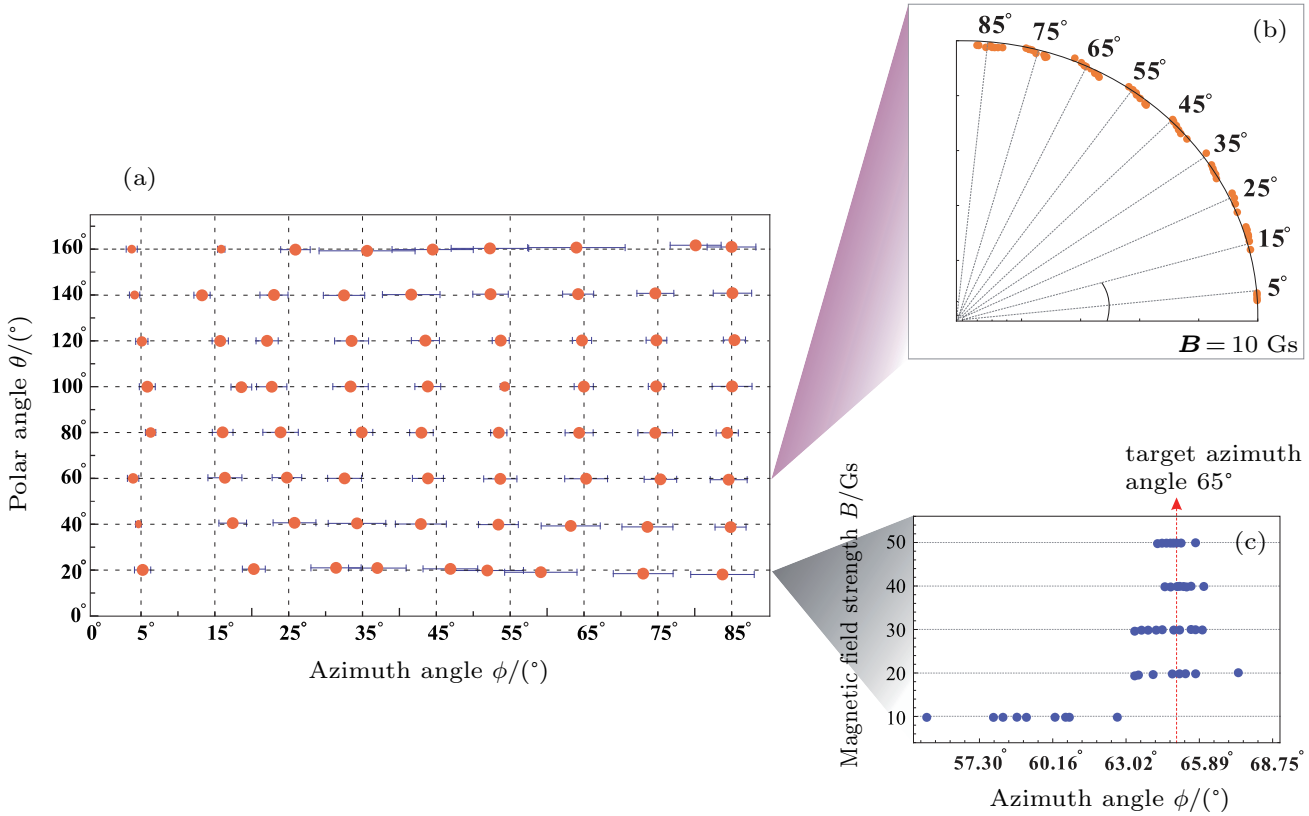


Fig. 6. (color online) (a) The detected magnetic field strength is set to 10 Gs. Each simulated azimuth angle ϕ (5°–85° with 10° intervals) with error bar is obtained from corresponding formula $\xi_{\min}(\theta_0, \phi_0, B_0)$ with repetition cycles 10. The mean value of each cycle was obtained from 60 groups of random numbers ϵ_{ν_i} and ϵ_Δ, which are limited by linewidths $\delta\nu_i = 0.3$ MHz and $\delta\Delta = 26$ kHz, respectively. (b) As an example, the statistical distributions of simulated measurement of ϕ are demonstrated with $\theta = 60° \pm 0.2°$. (c) With the increasing magnetic field strength, relatively higher angle resolution of ϕ could be achieved. The searched target azimuth and polar angles are set to $\phi = 65°$ and $\theta = 20°$, respectively. Notations are defined in the main text.

Next, taking into account the errors $\pm\varepsilon_{ij}$ $(i, j = x, y, z)$ of hyperfine components referred in Appendix A, we found that for large misalignment angle θ relative to the NV–^{13}C axis, simulated field strength $\boldsymbol{B}$ and direction angle (θ, ϕ) were robust against these errors compared to those of small ones. Detailed numerical comparison would not be listed here.

2.5. The determination of vector magnetic field direction

Due to the mirror symmetry of NV–^{13}C, eight possible combinations of polar angles $(\theta, \pi - \theta)$ and azimuth angles $(\phi, \pi \pm \phi, 2\pi - \phi)$ correspond to nearly identical $\nu_{1,2,3,4}$ and Δ. However, for a definite NV–^{13}C hyperfine tensor, the polar angle θ could be firstly decided by observing relative fluorescence intensity of CW spectrums as shown in Fig. 4(a). More details refer to Appendix C. The eight possible directions could be narrowed down to four ones as illustrated in Fig. 7.

Finally, we propose a scheme that the authentic one of the four possible magnetic field directions could be singled out by observing their free dynamical evolutions $|\Psi_f^{(\mathrm{e,n})}(\tau)\rangle = \exp[-\mathrm{i}\mathcal{H}_{\mathrm{NV}-^{13}\mathrm{C}}\tau]|\Psi_\mathrm{i}^{(\mathrm{e,n})}\rangle$ of initial states $|\Psi_\mathrm{i}^{(\mathrm{e,n})}\rangle = |\psi^{(\mathrm{e})}\rangle \otimes |\psi_{1\text{ or }2}^{(\mathrm{n})}\rangle$ under the Hamiltonian (2). The initial electron spin state $|\psi^{(\mathrm{e})}\rangle$ could be prepared in $(|m_\mathrm{s} = 0\rangle + |m_\mathrm{s} = -1\rangle)/\sqrt{2}$ and initial ^{13}C nuclear spin state $|\psi_1^{(\mathrm{n})}\rangle = (|m_I = +1/2\rangle + |m_I = -1/2\rangle)/\sqrt{2}$ or $|\psi_2^{(\mathrm{n})}\rangle = (|m_I = +1/2\rangle - \mathrm{i}|m_I = -1/2\rangle)/\sqrt{2}$, respectively. Finally, $|\Psi_\mathrm{f}^{(\mathrm{e,n})}(\tau)\rangle$ is projected into ground state $|\eta\rangle = |m_\mathrm{s} = 0\rangle \otimes |m_I = -1/2\rangle$ with $p(\tau) = |\langle\eta|\Psi_\mathrm{f}^{(\mathrm{e,n})}(\tau)\rangle|^2$. The resulting population evolutions $p(\tau)$ under different initial ^{13}C nuclear spin state $|\psi_{1\text{ or }2}^{(\mathrm{n})}\rangle$ could exclude the symmetrical solutions of four azimuth angles ϕ as shown in Fig. 8. The envelopes contain rapid oscillations, which are from the term of zero-field splitting D in the laboratory frame. In experiment, FID signal could be measured.

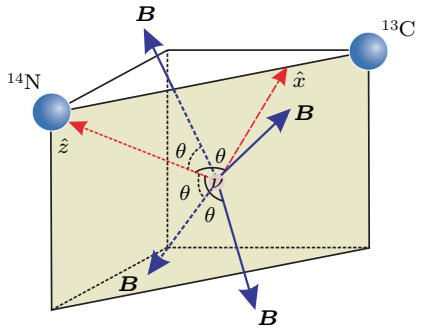


Fig. 7. (color online) Four possible magnetic field directions satisfying mirror symmetry about the x–z plane correspond to the same CW resonance spectrum and Larmor splitting.

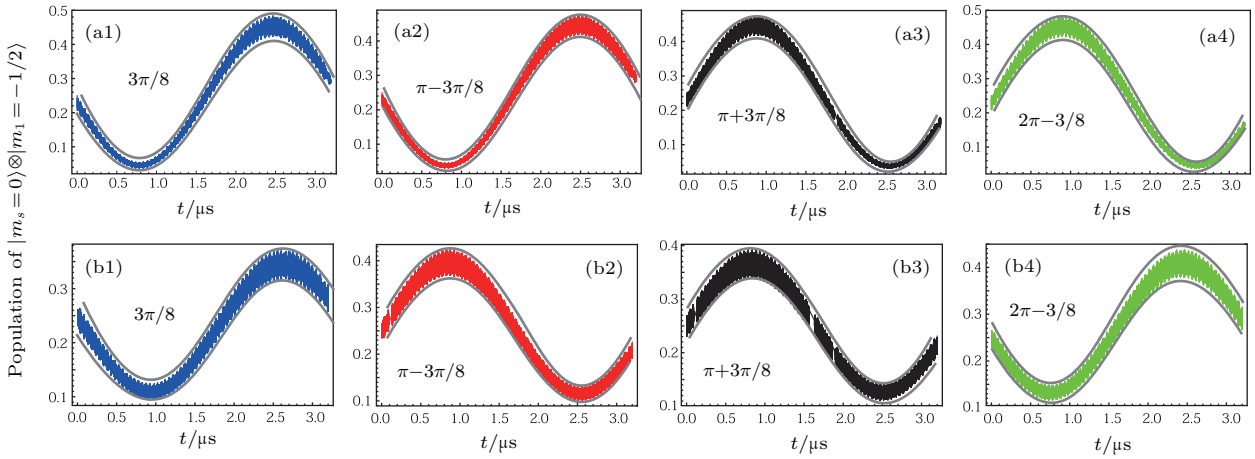


Fig. 8. (color online) As an example, both the vector magnetic field strength and the four possible directions have preset values $\boldsymbol{B} = 12$ Gs, $\theta = 3\pi/16$, and four possible azimuth angle $\phi = 3\pi/8$, $\pi \pm 3\pi/8$, or $2\pi - 3\pi/8$ satisfying mirror symmetry about ^{14}N–V–^{13}C plane. The four possible angles could be clearly discriminated by the evolutionary processes of preparing two different initial nuclear spin state $|\psi_{1\text{ or }2}^{(n)}\rangle$. The probability evolution is shown by the envelope. (a1)–(a4), the initial state $|\Psi^{(e)}\rangle \otimes |\psi_1^{(n)}\rangle$; (b1)–(b4), the initial state $|\Psi^{(e)}\rangle \otimes |\psi_2^{(n)}\rangle$. Notations are defined in the main text.

3. Conclusion

In this paper, we proposed an experimental scheme implementable with current technology, which could detect a static vector magnetic field including both strength and vector directions by employing the NV center with a first-shell ^{13}C nuclear spin. Based on the hyperfine tensors between an electron and a single nearest-neighbor ^{13}C nucleus, we could acquire the desired information of the vector field by observing the CW ODMR spectrums of hyperfine splitting induced by both ^{14}N and ^{13}C nucleus. Compared with the previous methods of multi-NV magnetometer, our scheme provides a potential alternative method and may enhance the angular resolution for the inhomogeneous magnetic field in space.

Appendix A: Eigenstate probability amplitude on the basis $|\ell, \alpha_k\rangle$ of sub-manifold $m_s = \pm 1$

The eigenvalues of Hamiltonian $\mathcal{H}_{\text{NV}-^{13}\text{C}} = DS_z^2 + \gamma_e \boldsymbol{B} \cdot \boldsymbol{S} + \gamma_n^{^{13}\text{C}} \boldsymbol{B} \cdot \boldsymbol{I}^{^{13}\text{C}} + \boldsymbol{S} \cdot \boldsymbol{A} \cdot \boldsymbol{I}^{^{13}\text{C}}$ in descending order correspond to the eigenvectors $|E_{j=1,2,3,4}\rangle$ and $|E_{i=5,6}\rangle$ of sub-manifold $m_s = \pm 1$ and $m_s = 0$, respectively. The quantity $|\langle E_j|\ell, \alpha_k\rangle|^2$ represents eigenstate probability on the basis $|\ell, \alpha_k\rangle$ of sub-manifold $m_s = \pm 1$.

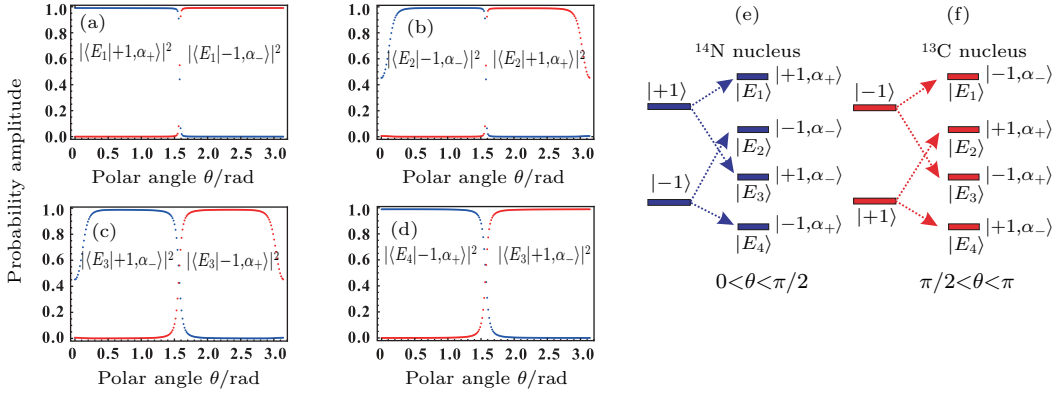


Fig. A1. (color online) (a)–(d) The $|\langle E_j|\ell, \alpha_k\rangle|^2$ shows eigenstate probability on the basis $|\ell, \alpha_k\rangle$ of sub-manifold $m_s = \pm 1$. (e), (f) Schematic energy level diagrams of an NV–^{13}C show that the eigenvectors $|\ell, \alpha_k\rangle$ would exchange when polar angle θ crosses over the sudden change point $\pi/2$ as shown in panels (a)–(d), where ϕ is set to 1.26 rad and hyperfine tensor is $\boldsymbol{A}_1$ with $A_{xz} = 24.1$ MHz. Similar results could be obtained from other candidate hyperfine tensors.

Appendix B: The determination of hyperfine tensors for NV–^{13}C for concrete experiment

Due to C_s symmetry of NV–^{13}C, eight possible hyperfine tensors are listed in Table B1.

Table B1. Hyperfine components (MH$_2$) for NV–^{13}C.

	$A_{xx}(\pm\varepsilon_{xx})$	$A_{yy}(\pm\varepsilon_{yy})$	$A_{zz}(\pm\varepsilon_{zz})$	$A_{xz}(\pm\varepsilon_{xz})$
$\mathcal{A}_1$	189.3(±1.1)	128.4(±1.0)	128.9(±4.3)	±24.1(±1.2)
$\mathcal{A}_2$	–189.3(±1.1)	128.4(±1.0)	–128.9(±4.3)	∓24.1(±1.2)
$\mathcal{A}_3$	–163.0(±2.4)	–128.4(±1.0)	85.7(±3.3)	∓99.3(±2.8)
$\mathcal{A}_4$	163.0(±2.4)	–128.4(±1.0)	–85.7(±3.3)	±99.3(±2.8)

Appendix C: MW transition matrix element

The MW transition matrix element $|\langle E_j|S_x|E_i\rangle|^2$ with $j = 1,2,3,4$ and $i = 5,6$ could qualitatively reveal the differences of resonance intensity, which should be sensitive to the polar angle θ of an applied static vector magnetic field.

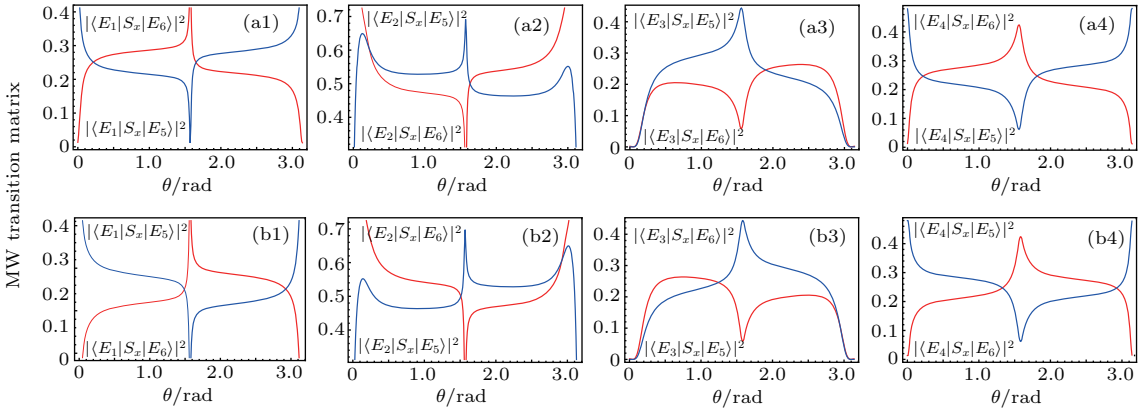


Fig. C1. (color online) The MW transition matrix elements $|\langle E_j|S_x|E_i\rangle|^2$, being a function of polar angle θ with a fixed azimuth angle $\phi = 1.26$ rad and $\boldsymbol{B} = 21$ Gs, reveal the relative intensities of fluorescence for the doublet transition of $|0,\beta_\pm\rangle \leftrightarrow |\ell,\alpha_k\rangle$ under low power microwave. Red and blue lines represent the relatively higher frequency transition $|0,\beta_-\rangle \leftrightarrow |\ell,\alpha_k\rangle$ and lower frequency transition $|0,\beta_+\rangle \leftrightarrow |\ell,\alpha_k\rangle$, respectively. (a1)–(a4): $\boldsymbol{A}_1$ with $A_{xz} = 24.1$ MHz; (b1)–(b4): $\boldsymbol{A}_1$ with $A_{xz} = -24.1$ MHz.

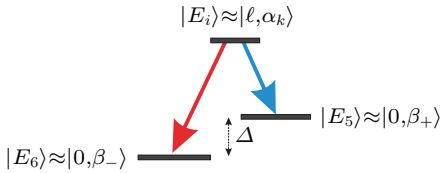


Fig. C2. (color online) Red and blue arrow lines represent the relatively higher frequency transition $|0,\beta_-\rangle \leftrightarrow |\ell,\alpha_k\rangle$ and lower frequency transition $|0,\beta_+\rangle \leftrightarrow |\ell,\alpha_k\rangle$, respectively.

Acknowledgment

We thank Ke-Biao Xu, Peng-Fei Wang, and Fa-Zhan Shi for helpful discussions.

References

[1] Doherty M W, Manson N B, Delaney P, Jelezko F, Wrachtrupe J and Hollenberg L C L 2013 *Phys. Rep.* **528** 1
[2] Suter D and Jelezko F 2017 *Progress in Nuclear Magnetic Resonance Spectroscopy* **98–99** 50
[3] Neumann P, Mizuochi N, Rempp F, Hemmer P, Watanabe H, Yamasaki S, Jacques V, Gaebel T, Jelezko F and Wrachtrup J 2008 *Science* **320** 1326
[4] Jiang L, Hodges J S,Maze J R, Maurer P, Taylor J M, Cory D G, Hemmer P R, Walsworth R L, Yacoby A, Zibrov A S and Lukin M D 2009 *Science* **326** 267
[5] Shi F Z, Rong X, Xu N Y, Wang Y, Wu J, Chong B, Peng X H, Kniepert J, Schoenfeld R, Harneit W, Feng M and Du J F 2010 *Phys. Rev. Lett.* **105** 040504
[6] Maurer P C, Kucsko G, Latta C, Jiang L, Yao N Y, Bennett S D, Pastawski F, Hunger D, Chisholm N, Markham M, Twitchen D J, Cirac J I and Lukin M D 2012 *Science* **336** 1283
[7] Rong X, Geng J P, Wang Z X, Zhang Q, Ju C Y, Shi F Z, Duan C K and Du J F 2014 *Phys. Rev. Lett.* **112** 050503
[8] Chen Q, Feng M, Du J F and Hai W H 2011 *Chin. Phys. B* **20** 010308
[9] Maze J R, Stanwix P L, Hodges J S, Hong S, Taylor J M, Cappellaro P, Jiang L, Gurudev Dutt M V, Togan E, Zibrov A S, Yacoby A, Walsworth R L and Lukin M D 2008 *Science* **455** 644
[10] Balasubramanian G, Chan I Y, Kolesov R, AlHmoud M, Tisler J, Shin C, Kim C D, Wojcik A, Hemmer P R, Krueger A, Hanke T, Leitenstorfer A, Bratschitsch R, Jelezko F and Wrachtrup J 2008 *Nature* **455** 648
[11] Shi F Z, Zhang Q, Wang P F, Sun H B, Wang J, Rong X, Chen M, Ju C Y, Reinhard F, Chen H W, Wrachtrup J, Wang J F and Du J F 2015 *Science* **347** 1135
[12] Gruber A, Dräbenstedt A, Tietz C, Fleury L, Wrachtrup J and Borczyskowski C V 1997 *Science* **276** 2012
[13] Wang P F, Yuan Z H, Huang P, Rong X, Wang M Q, Xu X K, Duan C K, Ju C Y, Shi F Z and Du J F 2015 *Nat. Commun.* **6** 6631
[14] Xu N Y, Jiang F J, Tian Y, Ye J F, Shi F Z, Lv H J, Wang Y, Wrachtrup J and Du J F 2016 *Phys. Rev. B* **93** 161117
[15] Maertz B J, Wijnheijmer A P, Fuchs G D, Nowakowski M E and Awschalom D D 2010 *Appl. Phys. Lett.* **96** 092504
[16] Lee S Y, Niethammer M and Wrachtrup J 2015 *Phys. Rev. B* **92** 115201
[17] Simanovskaia M, Jensen K, Jarmola A, Aulenbacher K, N. Manson and Budker D 2013 *Phys. Rev. B* **87** 224106
[18] Shim J H, Nowak B, Niemeyer I, Zhang J, Brandäo F D and Suter D arXiv: 13070257v2 [quant-ph].
[19] Rao K R K and Suter D 2016 *Phys. Rev. B* **94** 060101.
[20] Dreau A, Maze J R, Lesik M, Roch J F, and Jacques V 2012 *Phys. Rev. B* **85** 134107
[21] Nizovtsev A P, Kilin S Ya, Pushkarchuk V A, Pushkarchuk A L and Kuten S A 2010 *Opt. Spectrosc.* **108** 230
[22] Greau A, Lesik M, Rondin L, Spinicelli P, Arcizet O, Roch J F and Jacques V 2011 *Phys. Rev. B* **84** 195204
[23] Felton S, Edmonds A M, Newton M E, Martineau P M, Fisher D, Twitchen D J and Baker J M 2009 *Phys. Rev. B* **79** 075203
[24] Alvarez G A, Bretschneider C O, Fischer R, London P, Kanda H, Onoda S, Isoya J, Gershoni D and Frydman L 2015 *Nat. Commun.* **6** 8456
[25] Childress L, Gurudev Dutt M V, Taylor J M, Zibrov A S, Jelezko F, Wrachtrup J, Hemmer P R and Lukin M D 2006 *Science* **314** 281